

Mechanisms of material removal and subsurface damage in fixed-abrasive diamond wire slicing of single-crystalline silicon

Takaaki Suzuki^{a,b}, Yuki Nishino^b, Jiwang Yan^{c,*}

^a Graduate School of Science and Technology, Keio University, 3-14-1, Hiyoshi, Kohoku-ku, Yokohama, 223-8522, Japan

^b READ Co., Ltd., 144-7, Tateuchi, Ohkuma Usibukuro, Watari-cho, Miyagi, 989-2302, Japan

^c Department of Mechanical Engineering, Keio University, 3-14-1, Hiyoshi, Kohoku-ku, Yokohama, 223-8522, Japan

ARTICLE INFO

Article history:

Received 10 April 2017

Accepted 19 April 2017

Available online 23 April 2017

Keywords:

Fixed abrasive
Diamond wire
Precision slicing
Single-crystal silicon
Dicing wire saw
Ductile mode machining
Subsurface damage
Surface integrity

ABSTRACT

Single-crystal silicon was sliced using a newly developed high-speed fixed-abrasive dicing wire saw. The effects of diamond grit size, wire speed, and number of slicing cycle on the surface roughness and subsurface damage of the workpiece were investigated by surface profiling, Raman spectroscopy and cross-sectional transmission electron microscopy. It was found that by using finer diamond grits and increasing the sawing cycles, the depth of micro dents and saw marks was reduced significantly, and in turn, the surface roughness was improved. A transition from brittle mode to ductile mode machining was confirmed from chip morphology observation when reducing the grit size. The subsurface damaged layers were composed of amorphous layers, dislocated layers with grain boundaries, as well as micro cracks. The smooth surface regions were dominated by amorphous silicon; while within the saw marks, a mixture of amorphous and metastable silicon phases was detected. Inside the micro dents, however, single-crystal silicon was predominant. Furthermore, the significance of silicon amorphization and poly-crystallization was strongly dependent on the wire speed. The higher the wire speed, the less the amorphous and polycrystalline layer. The present study provides comprehensive insights into the surface formation mechanism which is important for process optimization of high-speed and low-damage slicing of single-crystal silicon.

© 2017 Elsevier Inc. All rights reserved.

1. Introduction

In recent years, globally, there has been increased interest in solar power generation, and its implementation is becoming more widespread [1]. There is a long history of using single-crystal silicon substrates for solar cell modules, and silicon is still the most common material used for this purpose owing to its high efficiency in power generation. Thousands of wafers can be obtained at one time by slicing through a silicon ingot using a multi-wire saw. In the past, a method called free-abrasive machining, where running wires transported slurry containing SiC grits suspended in the grinding fluid, had been used in the sawing process. However, currently the sawing method using fixed-abrasive diamond wires has partially replaced the free-abrasive method [2,3]. In particular, the machining speed when using the electroplated fixed abrasive wires is over three times faster compared to the free-abrasive machining method. Fixed-abrasive wire sawing also has an advantage of min-

imizing kerf loss because the abrasive grits are fixed and held in place [4–8].

In addition, there is a need to make wafers thinner in order to reduce the weight of solar cells. For extremely thin wafers, it is important to realize high-precision slicing to prevent wafer breakage; thus, it is essential to understand the surface formation mechanism and structures of process-affected layers during machining. The depth of subsurface damage also affects the etching process that comes after slicing. Up to now, many studies have focused on evaluating the wafer thickness, waviness and surface roughness after sawing, but few have focused on the process-affected layers, i.e., the subsurface damage.

The purpose of this study is to improve the surface integrity of single-crystal silicon when it is sliced using the fixed-abrasive diamond wire sawing method. Especially, we experimented and studied how changing the abrasive grit size of the diamond wire as well as changing the wire speed in the machining condition influences the formation of the process-affected layer. The processing equipment used was a newly developed high-speed dicing wire saw which enables slicing through single-crystal silicon at a maximum wire speed of 1750 m/min [9]. Such high-speed slic-

* Corresponding author.

E-mail address: yan@mech.keio.ac.jp (J. Yan).

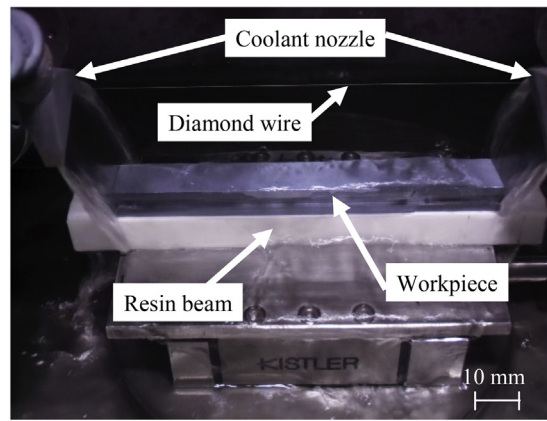
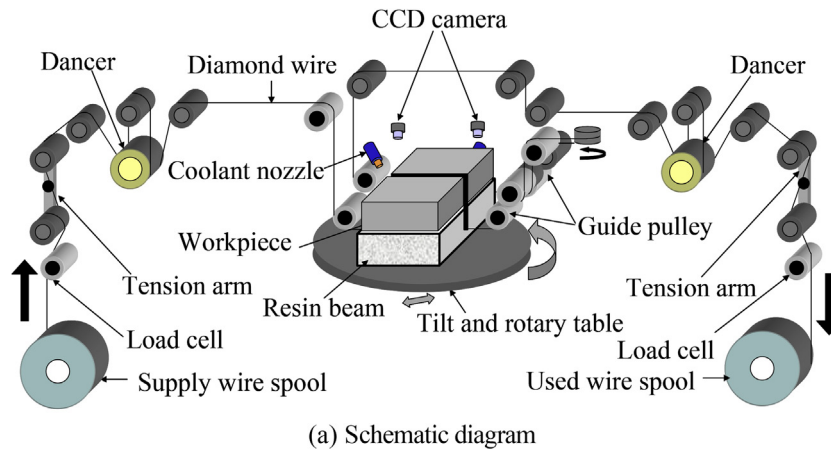


Fig. 1. Experimental setup of dicing wire saw: (a) schematic diagram. (b) close-up view.

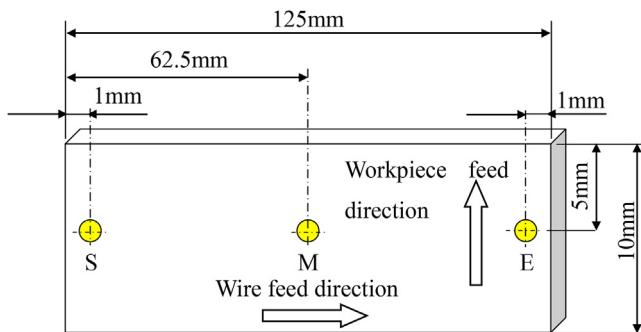


Fig. 2. Cross section of workpiece showing measurement points: wire entrance side (S), middle of the workpiece (M), wire exit side (E).

ing has never been reported in existing literature. In this paper, we will be reporting new findings regarding surface formation, material removal, process-affected layer structure, and wire topographical changes during high-speed silicon slicing using surface profiling, laser micro-Raman spectroscopy and transmission electron microscopy.

2. Experimental procedures

2.1. Experimental setup

The experiment was conducted using a newly developed dicing wire saw capable of high wire speed designed for fixed-abrasive

diamond wires. Fig. 1(a) is a schematic diagram of the experimental equipment, and Fig. 1(b) shows a photograph of a close-up view of the single-crystal silicon workpiece being sliced. With a lightweight and high precision bobbin unit, the equipment is designed to shorten acceleration and deceleration time and stabilize tension control, as well as wire speed control. The equipment is capable of slicing with up to two lines of wires simultaneously, while independently controlling tension for each of the wires. This equipment allows for the adjustment of the distance between the guide pulleys based on the width of the workpiece. It employs an up-cut method in which the workpiece rises, and is equipped with an upper charge-coupled device (CCD) camera and a rotary table enabling rapid alignment of workpiece. For this experiment, in order to better observe what occurs in high-speed slicing, we have selected to use only a single line in the machining process.

2.2. Slicing conditions

Table 1 shows the conditions for the slicing experiment. Ni-electroplated diamond wires were used. In order to investigate the impact of abrasive grit size, the diamond grits bonded to the diamond wires were of three size specifications: 5–10 μm , 6–12 μm , and 8–16 μm . The diamond grits are bonded to the wires at a density of approximately 1200 pieces/ mm^2 . The workpiece was a *p*-type single-crystal silicon with a specified shape (125 mm $W \times 10$ mm $H \times 13$ mm L), and tap water was used as the coolant. The wire speed was fixed at 1750 m/min, and the slicing process was repeated 15 times. Furthermore, in order to investigate the

Table 1
Experimental conditions.

Slicing parameters	Values
Wire speed (m/min)	1750 (for wires with diamond sizes of 5–10 μm and 8–16 μm) 750, 1000, 1250, 1500, 1750 (for wires with diamond size of 6–12 μm)
Tension (N)	11.76
Workpiece feed rate (mm/min)	12
Slicing depth (mm)	16.2
Wire length (m)	4000
Coolant	Tap water

impact of wire speed, we used the 6–12 μm grit size diamond wire to test five different wire speed settings and sliced 15 times under each condition. Under each slicing condition, the length of wire to be used per slice was set at 4000 m. Also, the diamond wires were sent in a single direction while slicing, from the supply spool to the worn wire spool; after slicing, the wires were rewound from the worn wire spool to the supply spool, reusing the same sections as the previous round.

2.3. Measurement and characterization

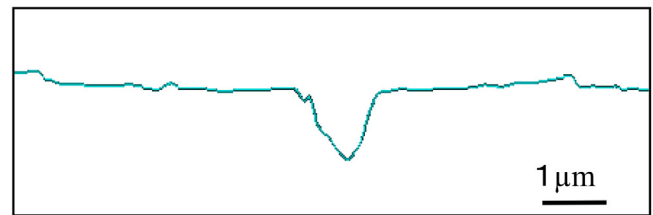
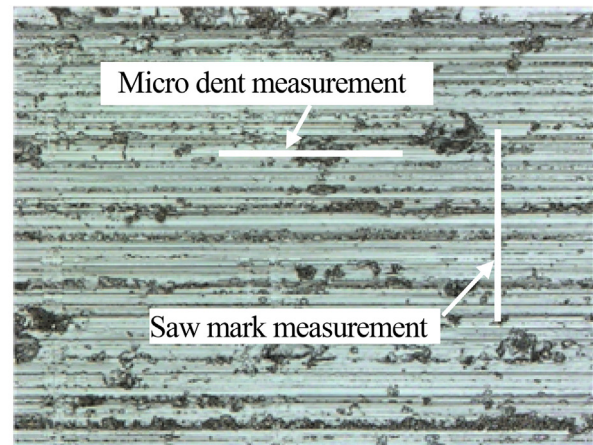
The surface roughness and micro dent depth of the workpiece after slicing, as well as the worn diamond wire's abrasive grit protrusion heights, were measured using a laser microscope (VK-9710, Keyence). Fig. 2 shows the measurement points of surface roughness. Starting from the side where the wire is fed to make contact with the workpiece, these points were designated as the wire entrance side (S), middle of the workpiece (M), and the wire exit side (E). The depths of micro dents and saw marks were measured at the middle of the workpiece M, and their values were based on a 10-point measurement average. Fig. 3 shows examples for measurement of depths of saw marks and micro dents.

The crystal structure of the machined surfaces was analysed using a laser micro-Raman spectrometer (NRS-3100, Jasco Corporation). The laser excitation wavelength was fixed at 532 nm, a 100 \times objective lens was used, and the laser beam diameter was 1 μm . A transmission electron microscope (TEM) (Tecnai G2 microscope, Philips N.V.) was used at an accelerating voltage of 200 kV to study the cross-sectional structure of the affected layers. The TEM samples were located in perpendicular to the wire feed direction at the middle section (M) of the machined workpiece. Fig. 4 shows where the cross-sectional TEM samples were cut out from the workpieces for observation. To prepare the TEM sample, we used focused-ion beam (FIB) milling to thin the sample to no more than 100 nm thick. Before FIB milling, the sample surfaces were coated with osmium and platinum to protect them from heat damage which could be caused by the ion beam. A scanning electron microscope (SEM) (VK-7800, Keyence) was used for observation of the diamond wires as well as the silicon chips removed during slicing.

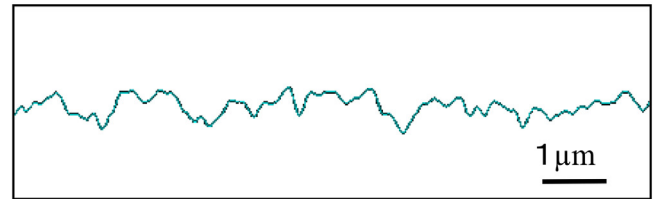
3. Results and discussion

3.1. Surface topography

Fig. 5 shows the changes in surface roughness R_a at the S (wire entrance side), M (middle of the workpiece), and E (wire exit side) points of the workpieces with respect to abrasive grit size and the line number, namely, the number of times the wires were used to slice (1, 5, 10, and 15 times). Comparing the first slice with the fifteenth slice, surface roughness decreased by a factor of three. It was



Depth of micro dent



Depth of saw mark

Fig. 3. Method for measuring the depth of micro dent and saw mark.

also noted that surface roughness results based on the machined locations S, M and E were nearly identical. This was most likely because after the wires were sent through in a single direction, they were fed back to the supply side before the next machining process began, and this process suppressed the potential variations that could have occurred with the protrusion heights caused by wear on the diamond particles over time with each usage. Furthermore, the results showed that the finer the abrasive grit size becomes, the more significantly smoother the surface becomes. This is likely because the finer the grit, the less variation there is in the protrusion heights stemming from the abrasive grit size distribution; thus, this reduces the depth of cut for a single abrasive grit, correspondingly, the surface roughness becomes smaller [10–13].

Fig. 6 shows laser microscope images of the workpiece surfaces after the first slice and the fifteenth slice, each sliced with various abrasive grit sizes at the wire speed of 1750 m/min. Each result showed saw marks in the direction the wires were fed, and the blue marks seen in the images were the micro dents found on the sliced surface. The micro dents were not location specific and appeared in random locations [14]. As a general trend, the number of indents within the measured area for the 15th line was smaller than that for the 1st line.

Fig. 7 shows the change in depth of the micro dents with abrasive grit size and line number, and Fig. 8 shows the corresponding change in depth of the saw marks. The depth of the micro dents was

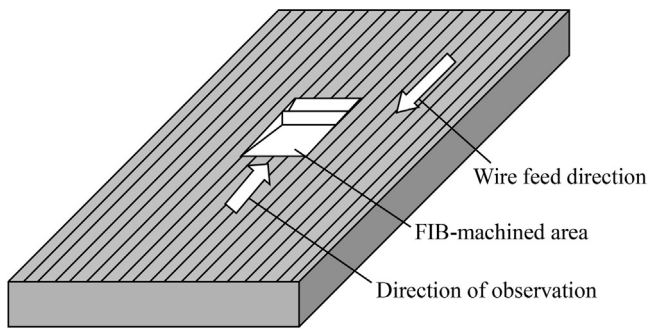
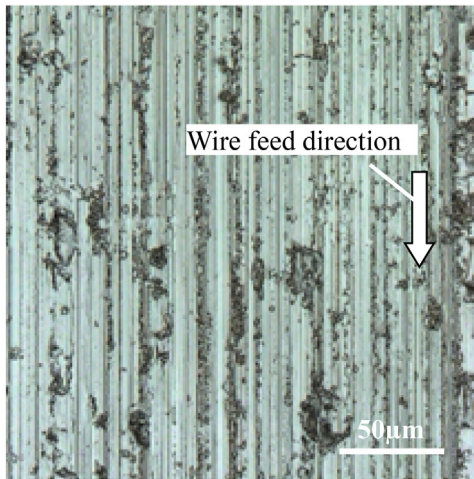


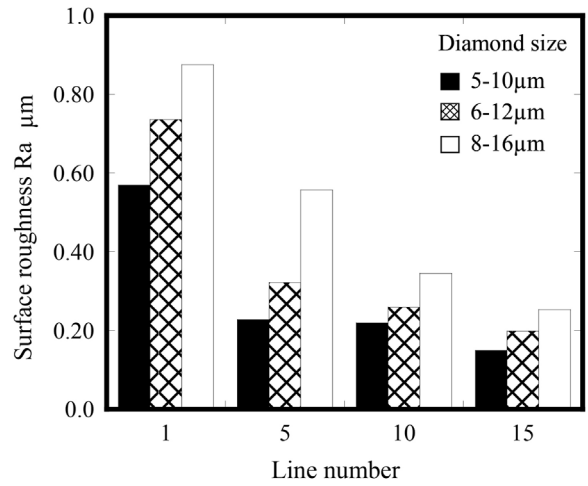
Fig. 4. Position of observation for cross section after slicing.

less than 700 nm with the 5–10 μm diamond grit size and less than 1100 nm with the 8–16 μm grit size. The finer the grits became, and the more times the wires were used to slice, the shallower the depths of the micro dents became; and in each case, after 15 slices, the dent depths were reduced to half of those in the first slice. In addition, the depth of the saw marks after 15 slices was less than 200 nm when the abrasive diamond grit size was 5–10 μm , and less than 300 nm when the abrasive grit size was between 8 and 16 μm . In addition, the dents were distinctly deeper than the saw marks.

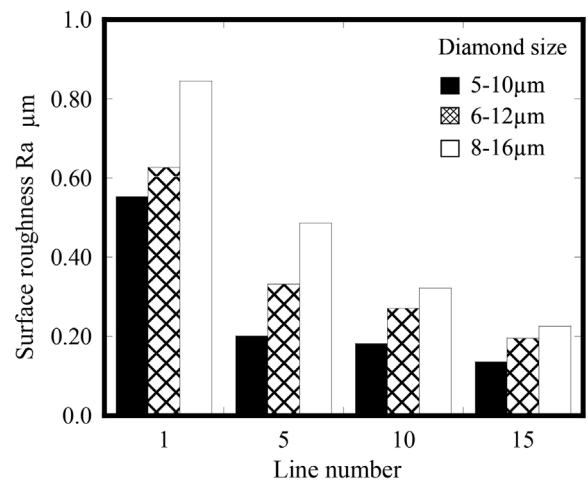
The micro dents are the results of microcracks that occur in single-crystal silicon during the slicing process and remained on the machined surface. Generally, the deeper each single abrasive grit cuts into silicon the more easily brittle fractures occur, and thus more and deeper micro dents occur [15–18]. In this research, the feeding speed is made constant in the direction of the cutting depth (z -direction), thus the depth of cut for each abrasive grit was reduced if finer grits are used. As a result, brittle fractures during machining were suppressed and the process would then transition to ductile mode machining [19,20]. Accordingly, the occurrence of micro dents was suppressed.

3.2. Raman spectroscopy

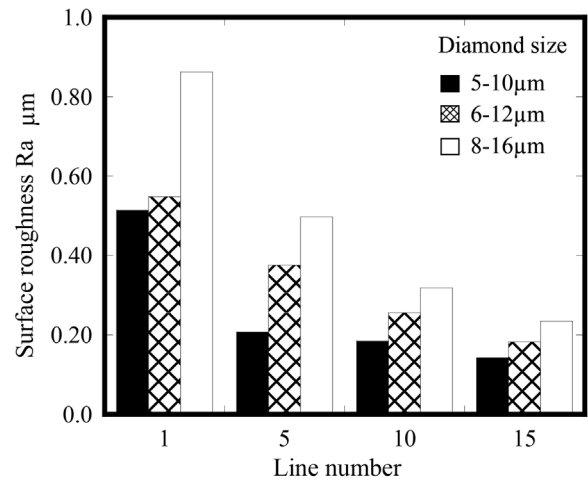
Fig. 9 shows typical results of Raman spectra for flat and smooth regions, saw marks, and micro dents on silicon surface after being sliced with diamond wires with abrasive grit size of 6–12 μm . For each spectrum, we saw a dominant peak near 520 cm^{-1} which is to say the surface is mainly in single-crystalline state (hereafter abbreviated as c-Si). However, near flat and smooth surface regions (Fig. 9(a)) and saw marks (Fig. 9(b)), it was found c-Si intensity was reduced, forming an amorphous silicon layer (hereafter abbreviated as a-Si) which peak at approximately 470 cm^{-1} . Particularly,



(a) Positions S



(b) Positions M



(c) Positions E

Fig. 5. Surface roughness at positions S, M, and E.

the c-Si intensity became relatively weaker where there were saw marks, while the a-Si peak became even stronger. Furthermore, in saw marks we observed a peak of Si-XII in a metastable phase near 352 cm^{-1} [21–24]. The generation of Si-XII phase might be a result of the intensive stress concentration around the tip of the diamond abrasive grains. This situation is different from that of the diamond

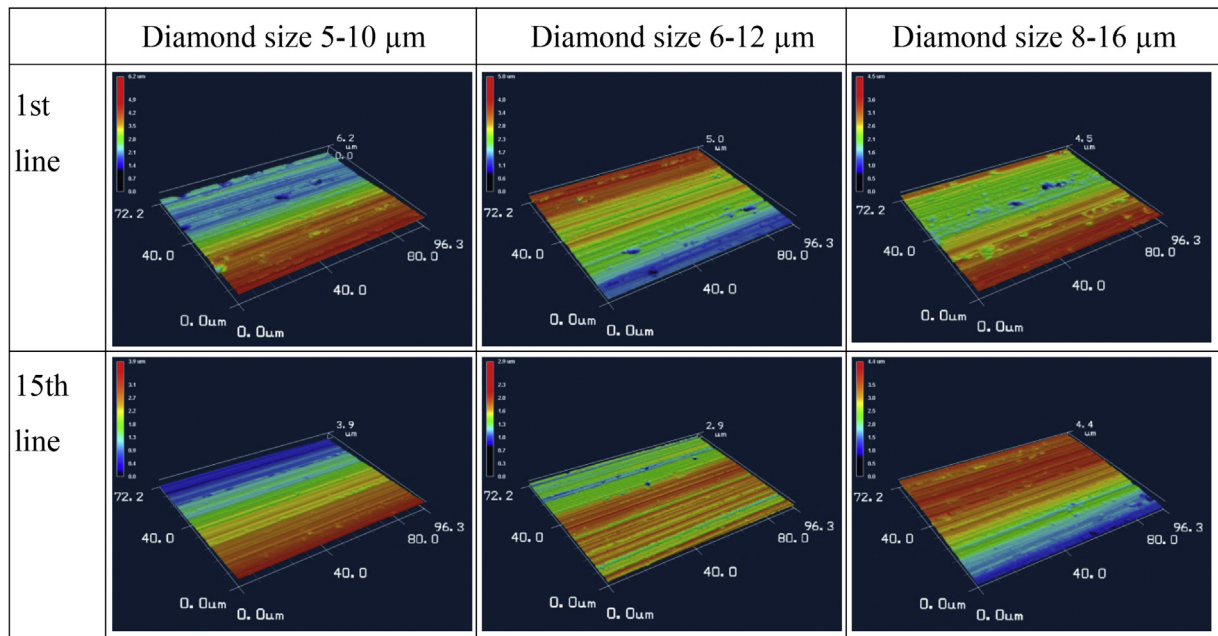


Fig. 6. Laser microscope images of silicon surface.

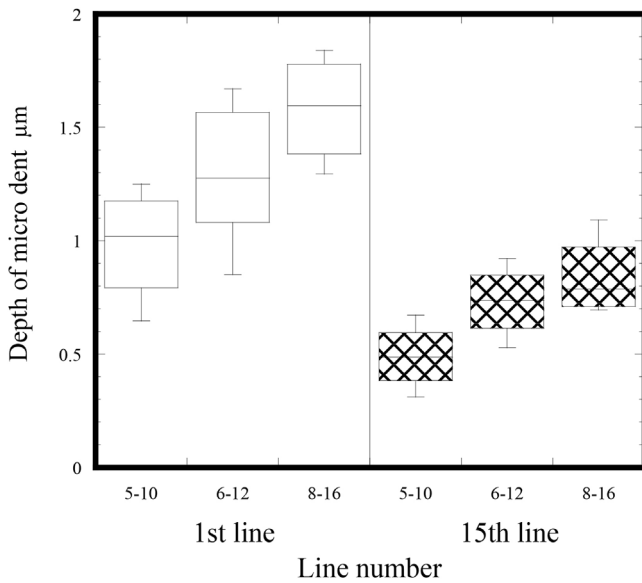


Fig. 7. Change in depth of micro dent with diamond size and line number.

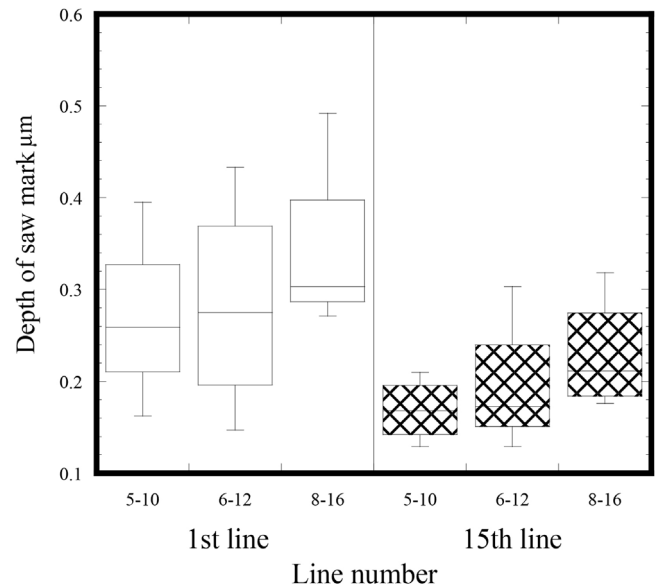


Fig. 8. Change in depth of saw mark with diamond size and line number.

turning process where a long cutting edge is used and the stress state is similar to the orthogonal cutting [25]. On the other hand, at the micro dent locations, c-Si peaks were more intense while other regions of the spectrum remained flat. This result confirms that because the depth of micro dents is more than twice that of saw marks, single-crystal silicon would form a brittle fracture and expose the crystallinity of the base Si (c-Si) to the machined surface [25–27].

Fig. 10 shows the results of Raman spectra of the smooth surface regions at the wire entrance side (S), when the diamond wire grit size was between 6 and 12 μm and machined at varied wire speeds. Regardless of which wire speed was used, a-Si peaks near 300 and 470 cm^{-1} were observed. Metastable phase Si-XII peaks at around 352 and 433 cm^{-1} were also observed. In addition, there is a tendency that the slower the wire speed, the greater the intensity of the a-Si peak. This result is likely because when the wire

speed is reduced, the deeper each of the abrasive grits cuts into the substrate in a ductile mode, and thus increases the thickness of the amorphous layer. Furthermore, at a low wire speed, the c-Si peak near 520 cm^{-1} is shifted toward a lower wavenumber, indicating that crystallinity was lowered and tensile stress remained after machining [28,29]. At 750 m/min, a polycrystalline silicon peak was observed at around 500 cm^{-1} , indicating poly-crystallization of single-crystalline silicon.

Fig. 11 shows the Raman spectra results of the smooth surface region at the wire entrance side, middle of the workpiece, and wire exit side when diamond grit size varied while wire speed remained constant at 1750 m/min. Amorphous phase, metastable phase Si-XII, and c-Si phase were observed, while hardly any difference was found in peak intensity dependent on abrasive grit size. On the other hand, from the viewpoints of different observation locations,

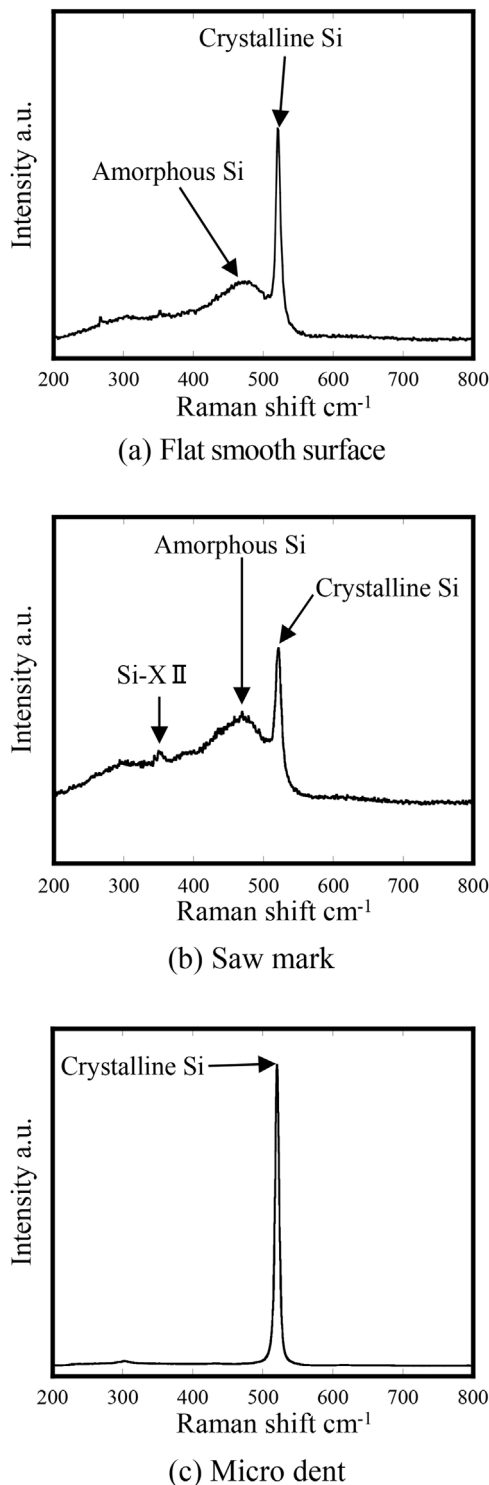


Fig. 9. Raman spectra of silicon surface at various positions.

it was found that the a-Si peak intensity had decreased towards the wire exit side following the wire feed direction.

To compare the intensities of Raman spectra from the amorphous region and that from the crystalline region, Raman intensity ratio r was defined in a previous study [25], as follows:

$$\gamma = I_a/I_c$$

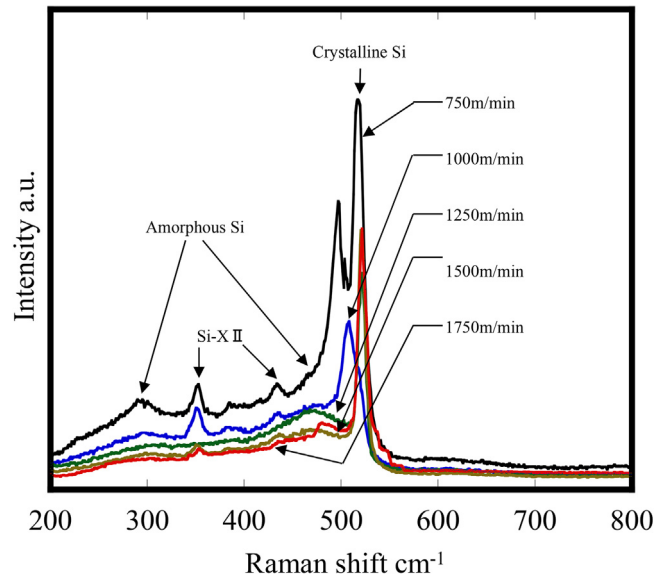


Fig. 10. Raman spectra of silicon surface at flat smooth surface of wire entrance side for diamond size of 6–12 μm at each wire speed.

where I_a is the total Raman intensity of the amorphous silicon, and I_c is the total Raman intensity of the crystalline silicon. The smaller the value of r , the thinner the amorphous layer.

Fig. 12 shows the Raman intensity ratios of the smooth surface regions at three different locations calculated from Fig. 11. The value of the Raman intensity ratio at the wire exit side was slightly smaller. This result showed a-Si phase at the wire exit side was weakened and c-Si phase became relatively strong. This would have been caused by that each of the abrasive grits cut in silicon deeper due to the progress of diamond grain exposure from the metal coating as it moved away from the entrance side. This, consequently, increased the number of brittle fractures and made the very surface of the workpiece show significant c-Si phase [30,31].

The aforementioned Raman spectroscopy analysis indicated that the flat and smooth surface regions of the workpiece is a mixture of c-Si, a-Si layer, and Si-XII phase, regardless of the abrasive grit size; and rather, when the wire speed was set to a slower one, it had relatively more impact on the formation of a-Si layer [32,33]. It also became clear that brittle mode machining causes micro dents, where crystalline silicon dominate the affected layer.

3.3. Cross-sectional TEM analysis

Fig. 13(a) shows a cross-sectional TEM image of the middle section of the workpiece after the fifteenth slice, where the slicing was conducted with 5–10 μm diamond grit size at a wire speed of 1750 m/min. The top side is the sample surface layer after machining, and the bottom side is the inside of the sample. The black region over the surface of the sample is osmium coating deposited as a protective layer in order to prevent FIB damage. The ring-like wrinkles seen at the upper region of the affected layer were caused by recovery of elastic deformation of the sample which is extremely thin. An a-Si layer (depth 100–200 nm) is observed at the uppermost surface and just below that we can see a few slip planes (dislocation bands) that were caused by the machining process. Below the dislocated region, there are a few downward extending microcracks [34–36]. The layer further below is the c-Si bulk. Fig. 13(b) shows a close-up view of the subsurface damage layers. The dislocated region and the cracked region consist of grain boundaries where submicron level micro crystals with different crystal orientations were observed, indicating poly-crystallization of silicon. This obser-

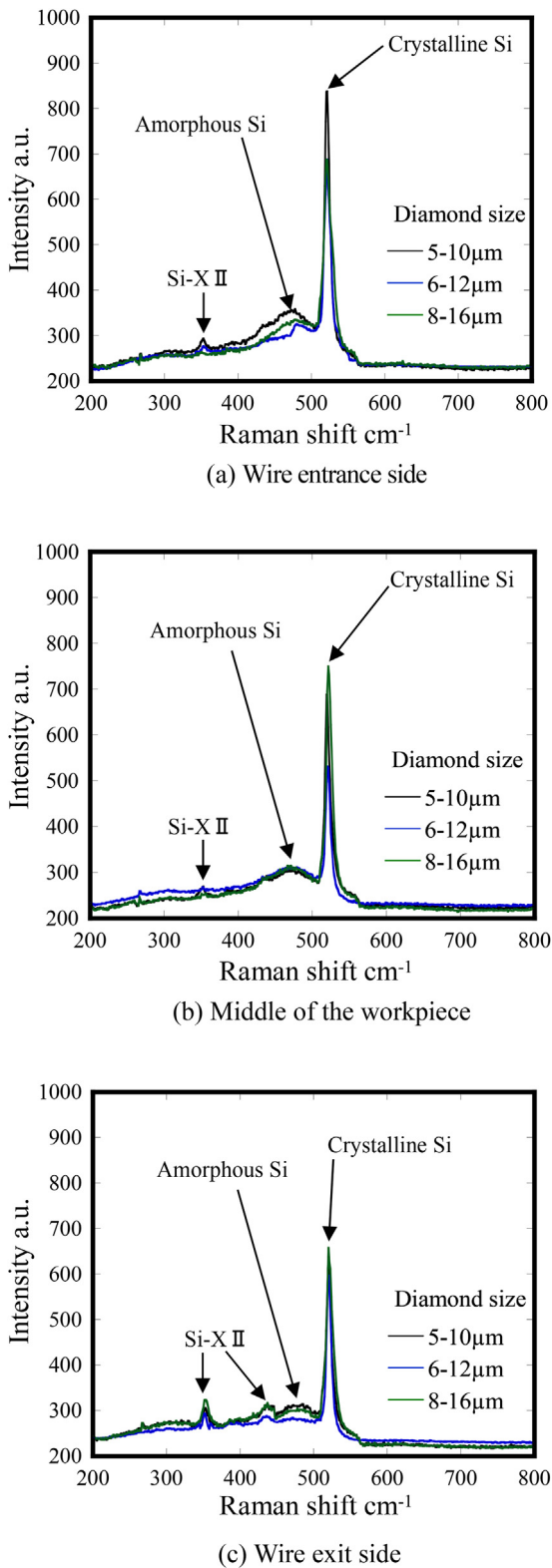


Fig. 11. Raman spectra of silicon surface at each position.

vation result agrees well with the Raman spectra shown in Fig. 10. The subsurface damage structure observed here is also similar to that of ultraprecision plunge cutting of silicon using a single-crystal diamond tool [37].

Fig. 14 shows magnified TEM image and fast Fourier transform (FFT) images of different subsurface regions. The FFT results were

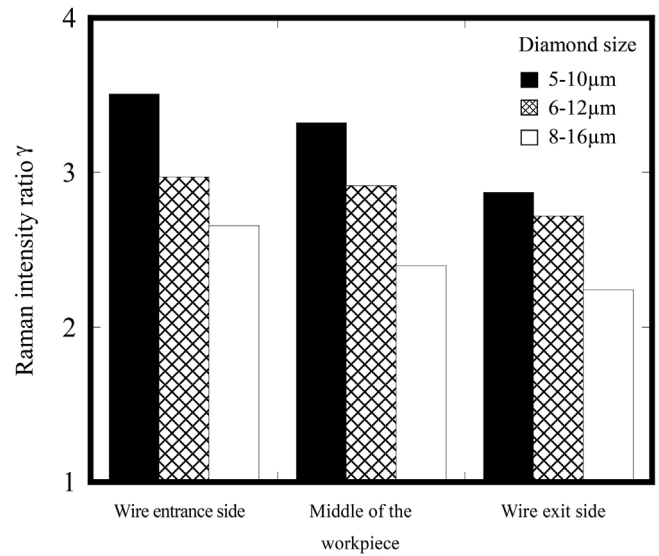


Fig. 12. Raman intensity ratio of silicon surface at each position.

Table 2
Result of the thickness of subsurface damage layers.

Item	Diamond size (μm)		
	5–10	6–12	8–16
Amorphous layer thickness (μm)	0.10–0.20	0.10–0.20	0.10–0.20
Dislocated layer thickness (μm)	0.40–0.80	0.50–0.90	0.60–1.10
Maximum lateral crack length (μm)	0.85	1.02	1.29

obtained using Gatan Micrograph software to analyse the digitised TEM images. For the a-Si layer, FFT results showed no clear light spots, but more a ring-like glow as seen in Fig. 14(b). The FFT results of the micro crystalline layer showed the crystalline structure distorted by severe strains, as seen in Fig. 14(c). Then, clear light spots are shown in the c-Si bulk region, as seen in Fig. 14(d). This indicates that Si crystalline structure is damaged to different extents by machining at various depth from the workpiece surface [38,39].

Fig. 15 shows TEM images of a cross section of a sample where the abrasive grit size was between 6 and 12 μm, and wire speed fed at 1750 m/min. The depth of the a-Si layer was between 100 and 200 nm. The subsurface structure including a-Si layer, dislocation lay, and microcracks are similar to those observed when diamond grit size between 5 and 10 μm was used (Fig. 13). Fig. 16 shows a magnified TEM image of the tip of a crack. This crack appears to be a median crack, and ripple-like rings could be observed near its tip [40–42]. The ripple-like rings are caused by the accumulation of internal stress taking place when the crack stops to propagate further [38,43].

Fig. 17 is a TEM image of a sample where the abrasive grit size was between 8 and 16 μm and the wire speed was 1750 m/min. There was a median crack that developed near a deformed region that occurred under the machined surface, and its length reached approximately 1.2 μm. The depth of a-Si layer was 100–200 nm, almost the same as when other abrasive grit sizes were used. Additionally, we observed at approximately 60 nm under the a-Si layer a poly-crystalline region, as shown in Fig. 17(c). As shown in Fig. 17(d), the crystal orientation of the micro crystal grains A and B are different near their boundary.

Table 2 shows a summary of the depth of a-Si layer, the depth of dislocated layer thickness, and the length of microcracks in relation to diamond grit size. The depth of the a-Si layer does not differ much based on abrasive grit size. On the other hand, the larger the diamond size becomes, the greater the depth where poly-crystalline

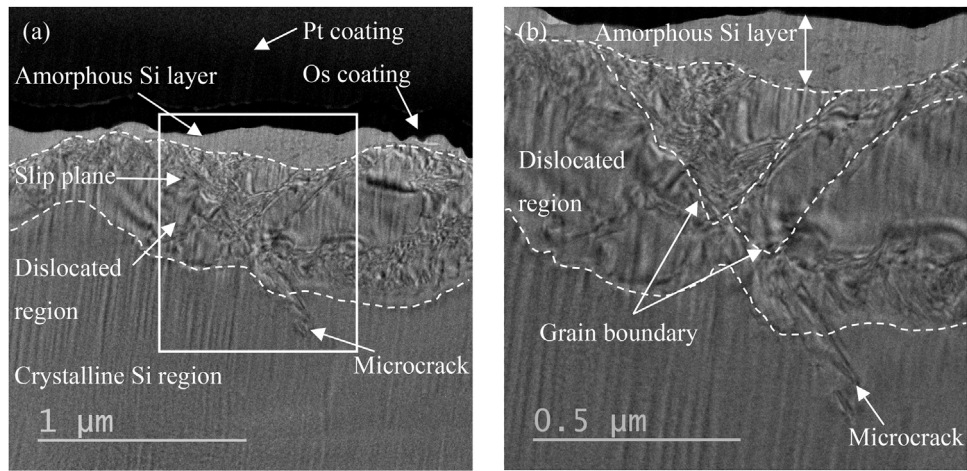


Fig. 13. (a) TEM image for diamond size of 5–10 μm , (b) enlarged view of the region outlined by the square in (a).

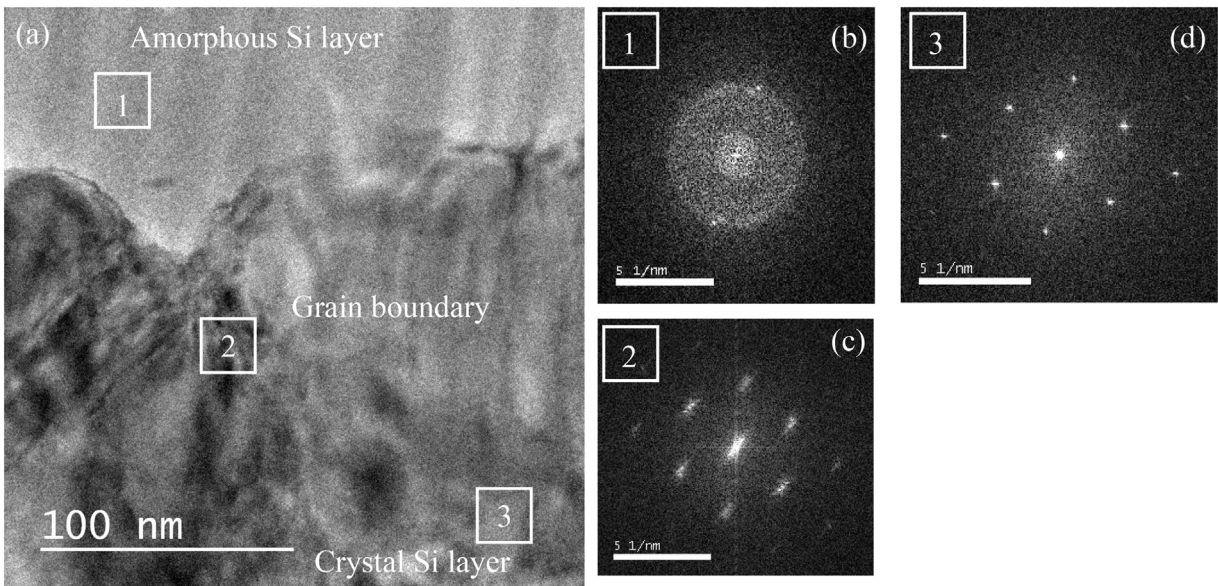


Fig. 14. (a) TEM image of near inter-phase boundary region, and FFT image (b) amorphous Si layer, (c) near the Grain boundary, (d) Crystallized Si layer.

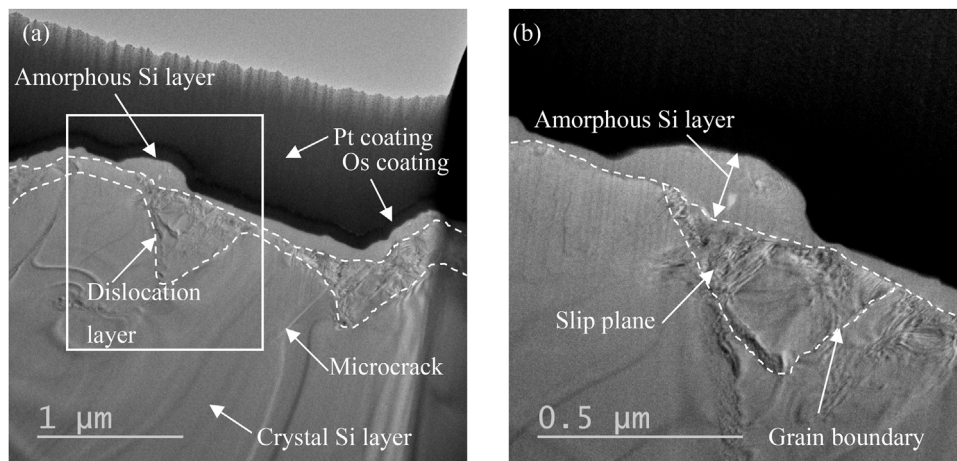


Fig. 15. (a) TEM image for diamond size of 6–12 μm , (b) enlarged view of the region outlined by the square in (a).

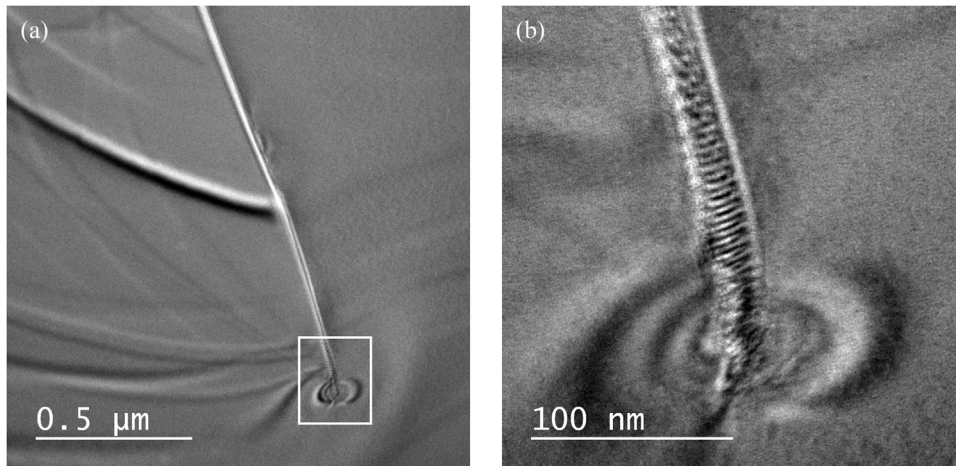


Fig. 16. (a) TEM image of the tip of the median crack, (b) enlarged view of the region outlined by the square in (a).

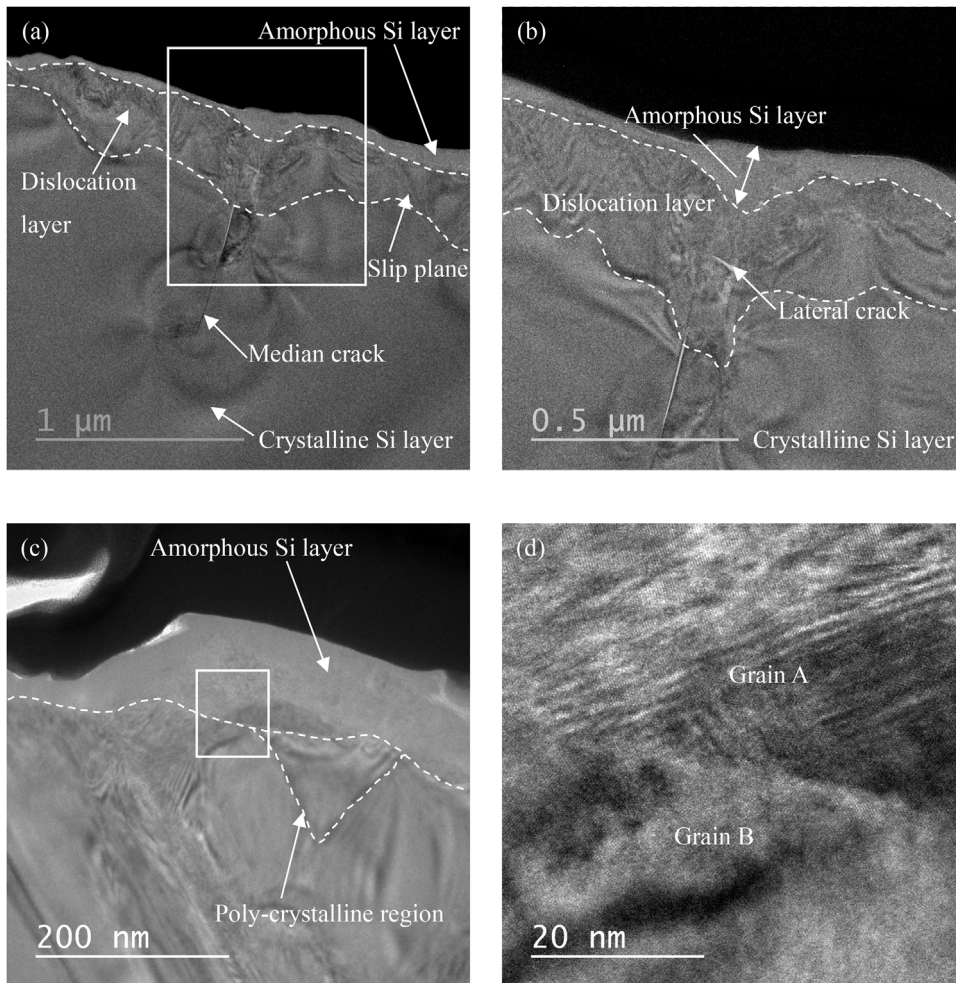
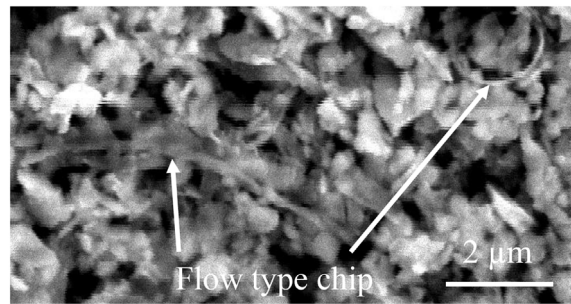
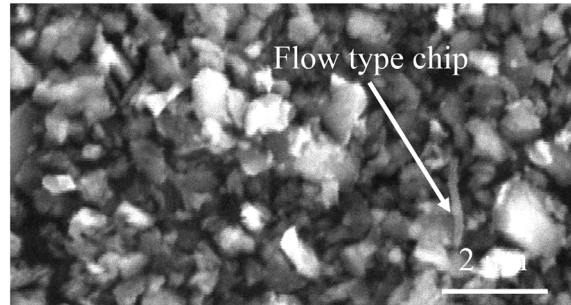
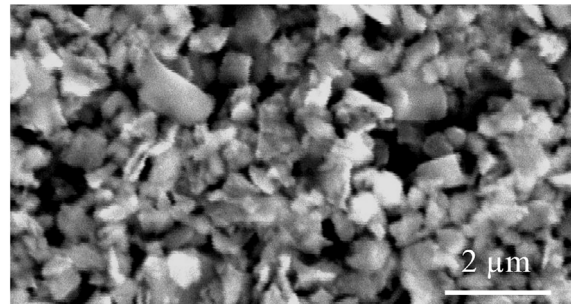


Fig. 17. (a) TEM image for diamond size of 8–16 μm , (b) enlarged view of the region outlined by the square in (a), (c) close-up view of amorphous Si layer, (d) enlarged view of the region outlined by the square in (c).

grains occurs, and the longer the microcracks become. From the viewpoint of nanoindentation, it is presumable that when machining begins with the abrasive grits and they are pushed into a brittle material, the material begins to deform plastically just below the contact area and cause median cracks below the deformed region in the vertical direction. Then, when the load is being removed from the substrate, the plastically deformed region and the elastically

deformed region around it would generate residual stress due to elastic recovery. This then becomes the driving force that generates a lateral crack in the material. When the abrasive grit size becomes larger, the depth of cut into the material becomes larger, and thus, the brittle fracture that is caused by the median and lateral cracks become more dominant [44–47]. Based on these results, it is indicated that using finer abrasive diamond grits would reduce the total

(a) Diamond size 5-10 μm (b) Diamond size 6-12 μm (c) Diamond size 8-16 μm **Fig. 18.** SEM images of chip at each diamond size.

depth of subsurface damaged layer, and reduce the time spent on chemical etching in the backend process.

3.4. Chip morphology

Fig. 18 shows SEM images of chips from the processes where various diamond sizes were used at a constant wire speed of 1750 m/min. The majority of the chip fragments were splinter-shaped (fracture type), but as the abrasive diamond grit size decreased, they became thinner and longer and took the form of flow type chips. The chip thickness was approximately 0.14 μm . It is likely that as the grit size decreases, the depth of cut for each grit also decreases, and that will cause a transition from a brittle fracture to plastic deformation, which will create flow type chips [48–50]. From this aspect, it is demonstrated again that when fine-grit diamonds were used, the material removal process transitioned from brittle mode machining to ductile mode machining [51–53].

3.5. Diamond wire topography

Fig. 19 shows SEM images of diamond wires for each grit size after they were used for a slicing distance of 1600 m. Though the

abrasive diamond grits were plated/wrapped with Ni to the metal wire, as the machining continued, the tip layer of the plating was ground down to become flat. The Ni-plating that covered the diamonds was partially removed and revealed the sharp protrusion of diamonds. Thus, it is presumable that in the wire slicing process, all the diamond grits on the wires are making full and even contact with the workpiece in a radial direction, and the wires are being twisted during slicing.

Fig. 20 shows the height of protrusion of the abrasive grit after machining process for wires with different diamond grit sizes. When the diamond size was between 5 and 10 μm , the protrusion was approximately 6 μm . Under this condition, as stated previously based on surface roughness and chip analysis results, the machining mode transitioned from a brittle mode to a ductile mode. Therefore, it is important to use diamond size between 5 and 10 μm , or much smaller, to obtain a sufficiently small grit protrusion for ductile mode slicing.

4. Conclusions

Using the newly developed high-speed dicing wire equipment, we conducted precision slicing experiments of single-crystal silicon

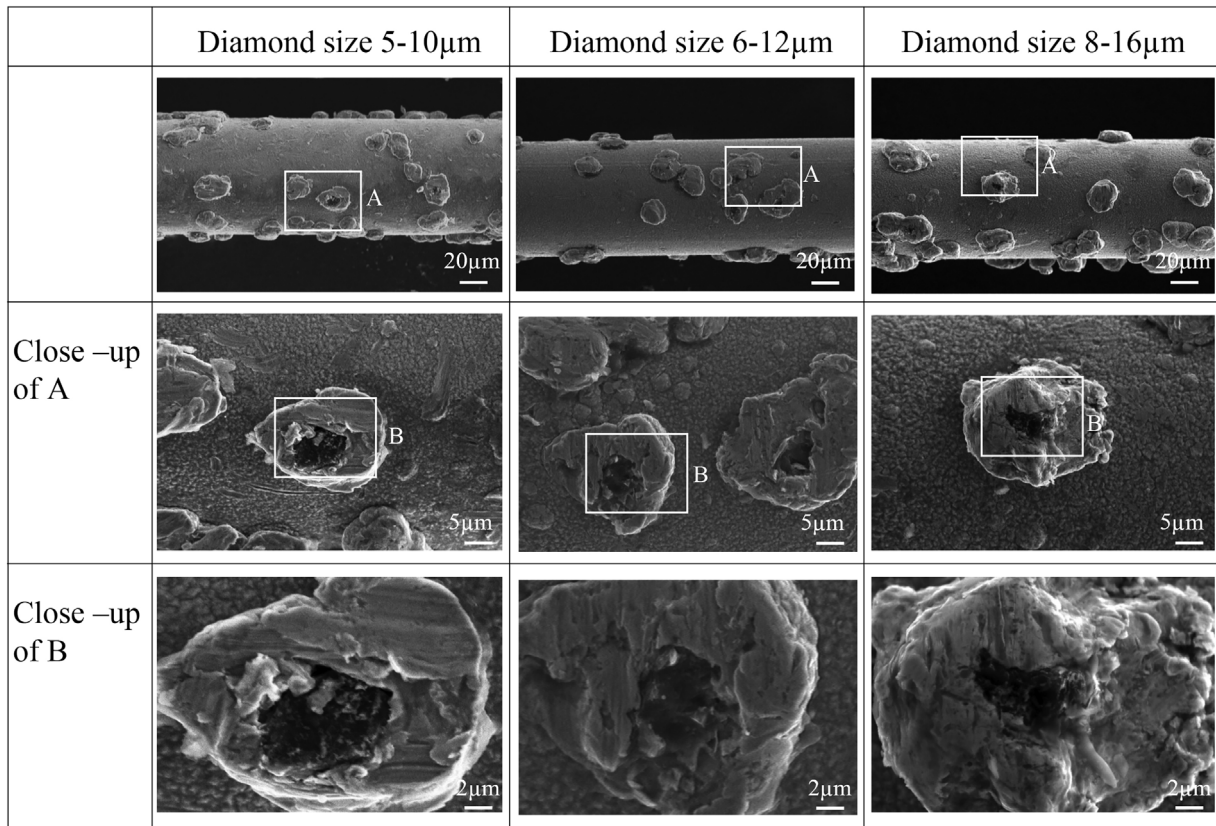


Fig. 19. SEM images of diamond wires for each diamond size.

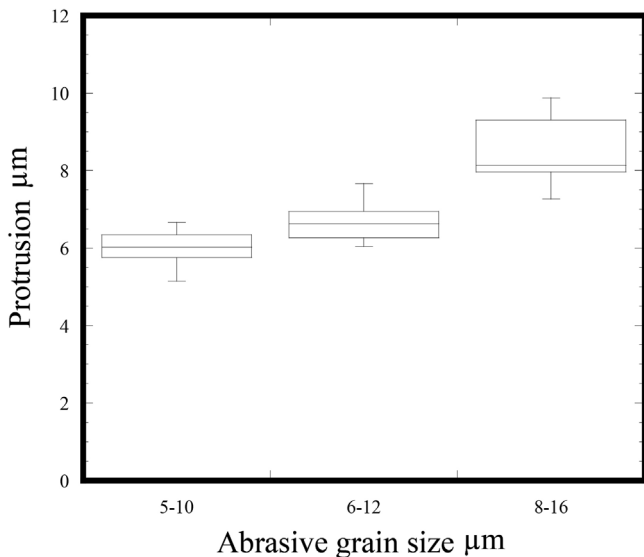


Fig. 20. Result of protrusion of diamond at a wire speed 1750 m/min.

under various slicing conditions to improve the surface integrity and reduce the process-affected layer. The following conclusions were obtained.

- 1) By using finer diamond grits, saw marks and micro dents were significantly reduced.
- 2) Surface roughness decreased with number of sawing cycles. As sawing cycle increased, the sharp tips of the diamond grits were rounded, leading to shallower/fewer saw marks and micro dents.

- 3) Raman spectroscopy results showed that the smooth surface areas and the saw marks had subsurface structure of a mixture of crystalline and amorphous silicon, while the micro dents had a crystalline structure. Metastable silicon phases were generated within the saw marks.
- 4) The significance of amorphous layer formation was independent of the abrasive grit size, but rather dependent on the wire speed. A low wire speed caused significant amorphization and polycrystallization of silicon.
- 5) TEM results illustrated that the subsurface damage layer was composed of an amorphous layer, a dislocated region below the amorphous layer, and microcracks below the dislocated region. When the abrasive grit size increased, the generation of microcracks became more significant, leading to brittle mode machining.
- 6) When finer diamond grains were used, flow-type chips were generated. Due to the decrease in undeformed chip thickness with the grit size, the machining mode transitioned from brittle to ductile.
- 7) Observation of the used wires showed that when the protrusion of the abrasive grit became less than approximately 6 μm , ductile-mode machined surface area increased. It was important to use diamond size between 5 and 10 μm , or much smaller, to obtain a sufficiently small grit protrusion for ductile mode slicing.

References

- [1] Japan Photovoltaic Energy Association. JPEA PV outlook 2030. Japan Photovoltaic Energy Association; 2015 [accessed 21 August 2016] <http://www.jpea.gr.jp/pdf/t120925.pdf>.
- [2] Oishi H, Asakawa K, Tsukamoto K, Uno Y. Study on abrasive grit size change and cutting mechanism in multiwire saw slicing—study on 400 mm-diameter silicon ingot slicing (3rd report). J Jap Soc Prec Eng 2001;67(6):891–6.

- [3] Suwabe H, Abe Y, Nirasawa K, Ishikawa K. Slurry behavior in slicing grooves with a multi-wire saw used for solar cells. *J Jap Soc Abrasive Technol* 2009;53(8):488–93.
- [4] Tanizaki A, Kawatsu T, Takata S, Sakata N. Wafer slicing with the wire of the silicon wafer for photovoltaics. *J Jap Soc Mech Eng* 2013;88:6–15.
- [5] Wang W, Liu ZX, Zhang W, Huang YH, Allen DM. Abrasive electrochemical multi-wire slicing of solar silicon ingots into wafers. *Manuf Technol* 2011;60:255–8.
- [6] Meinel B, Koschwitz T, Blocks C, Acker J. Comparison of diamond wire cut and silicon carbide slurry processed silicon wafer surfaces after acidic texturisation. *Mater Sci Semicond Process* 2014;26:93–100.
- [7] Yu Xuegong, Wang Peng, Li Xiaoqiang, Yang Deren. Thin Czochralski silicon solar cells based on diamond wire sawing technology. *Sol Energy Mater Sol Cells* 2012;98:337–42.
- [8] Meinel B, Koschwitz T, Acker J. Textual development of SiC and diamond wire sawed sc-silicon wafer. *Energy Procedia* 2012;27:330–6.
- [9] Suzuki T, Otsuki T, Yan J. Precision slicing of single-crystal silicon using a dicing wire saw. *J Jap Soc Abrasive Technol* 2016;60(2):97–103.
- [10] Honda R. Influence of elastic and plastic properties of work materials on ground surface roughness. *J Jap Soc Prec Eng* 1978;44(525):1057–63.
- [11] Zhang M, Sun Y, Zuo D, Xie C, Zhang C. Experimental study on slicing of sapphire with fixed abrasive diamond wire saw. *Int Sch Sci Res Innov* 2015;9:5.
- [12] Ichida Y, Kishi K, Hanida T, Iyori Y. Mirror finish grinding of β -sialon with fine grit ed diamond wheels. *Ceram Soc Jap* 1986;94(1):204–10.
- [13] Tso PL, Yan BH. A study of slicing process with thin diamond wire, international conference on leading edge manufacturing in 21st century. *Jap Soc Mech Eng* 2005:619–24.
- [14] Wu H. Wire sawing technology: a state-of-the-art review. *Prec Eng* 2016;43(1):1–9.
- [15] Jaeggi C, DeMeyer C, Wiedmer F, Stierli R, Simoncic P, Assi F, et al. Effects of wire lifetime in diamond wire wafering on the wafer roughness and mechanical strength. 27th European Photovoltaic Solar Energy Conference September 2012:1054–9.
- [16] Wu H, Yang C, Nelkote SN. Effect of reciprocating wire slurry sawing on surface quality and mechanical strength of as-cut solar silicon wafers. *Prec Eng* 2014;38(1):121–6.
- [17] Yan J, Syoji K, Kuriyagawa T. Effect of tool wear on diamond cutting of single crystal silicon. *Jap Soc Mech Eng* 2001;67(12):323–8.
- [18] Ichida Y, Kishi K, Hasuda Y. Optimum grinding condition for fine grit diamond wheels in precision grinding of ceramics. *Jap Soc Prec Eng* 1992;58(6):145–51.
- [19] Kumar A, Kaminski S, Melkote SN, Arcona C. Effect of wear of diamond wire on surface morphology, roughness and subsurface damage of silicon wafers. *Wear* 2016;364–365:163–8.
- [20] Buchwald R, Frohlich K, Wurzner S, Lehmann T, Sunder K, Moller HJ. Analysis of the sub-surface damage of mc- and cz- Si wafers sawn with diamond-plated wire. *Energy Procedia* 2013;38:901–9.
- [21] Bidville A, Wasmer K, Kraft R, Ballif C. Diamond wire-sawn silicon wafers—from the lab to the cell production. 24th European Photovoltaic Solar Energy Conference and Exhibition September 2009 2017.
- [22] Gogotsi YG, Domnich V, Dub SN, Kailer A, Nickel KG. Cyclic nanoindentation and Raman microspectroscopy study of phase transformations in semiconductors. *Mater Res* 2000;15(4):871–9.
- [23] Hu JZ, Merkle LD, Menoni CS, Spain IL. Crystal data for high-pressure phases of silicon. *Am Phys Soc* 1986;34(7):4679–84.
- [24] Gassilloud R, Ballif C, Gasser P, Buerki G, Michler J. Deformation mechanisms of silicon during nanoscratching. *Phys Stat Sol (a)* 2005;202(15):2858–69.
- [25] Yan J, Asami T, Kuriyagawa T. Nondestructive measurement of the machining-induced amorphous layers in single-crystal silicon by laser micro-Raman spectroscopy. *Prec Eng* 2008;32(3):186–95.
- [26] Yan J, Asami T, Harada H, Kuriyagawa T. Fundamental investigation on subsurface damage in single crystalline silicon caused by diamond machining. *Prec Eng* 2009;33(4):378–86.
- [27] Gogotsi Y, Zhou G, Ku Sang-Song, Cetinkunt S. Raman microspectroscopy analysis of pressure-induced metallization in scratching of silicon. *Semicond Sci Technol* 2001;16:345–52.
- [28] Gogotsi Y, Baek C, Kirscht F. Raman microspectroscopy study of processing-induced phase transformations and residual stress in silicon. *Semicond Sci Technol* 1999;14:936–44.
- [29] Kailer A, Gogotsi YG, Nickel KG. Phase transformations of silicon caused by contact loading. *J Appl Phys* 1997;81(7):3057–63.
- [30] Shimizu J, Zhou L, Onuki T, Ojima H, Yamamoto T, Suzuki N. Influence of affected layer in finishing process of Si wafer—examination by nanoscratching and molecular dynamics simulation. *J Jap Soc Abrasive Technol* 2011;55(11):662–7.
- [31] Yan J. Laser micro-Raman spectra of single-point diamond machined silicon substrates. *J Appl Phys* 2004;95(4):2094–101.
- [32] Gassilloud R, Ballif C, Gasser P, Buerki G, Michler J. Deformation mechanisms of silicon during nanoscratching. *Phys Stat Sol (a)* 2005;202(15):2858–69.
- [33] Jahg J, Lance MJ, Wen S, Tsui TY, Pharr GM. Indentation-induced phase transformations in silicon: influences of load, rate and indenter angle on the transformation behavior. *Acta Mater* 2005;53:1759–70.
- [34] Bhagavat S, Kao I. Theoretical analysis on the effects of crystal anisotropy on wiresawing process and application to wafer slicing. *Int J Mach Tool Manuf* 2006;46:531–41.
- [35] Chung C, Tsay GD, Tsai Meng-Hsiu. Distribution of diamond grits in fixed abrasive wire sawing process. *Int J Adv Manuf Technol* 2014;73:1485–94.
- [36] Shibata T, Fujii S, Makino E, Ikeda M. Ductile-regime turning mechanism of single-crystal silicon. *Prec Eng* 1996;18:129–37.
- [37] Yan J, Asami T, Harada H, Kuriyagawa T, Shimada S. Crystallographic effect on subsurface damage formation in silicon microcutting. *Ann CIRP Manuf Technol* 2012;61(1):131–4.
- [38] Tanaka H, Shimada S, Anthony L. Requirements for ductile-mode machining based on deformation analysis of mono-crystalline silicon by molecular dynamics simulation. *Ann CIRP* 2007;56(1):53–6.
- [39] Bradby JE, Williams JS, Wong-Leung J, Swain MV, Munroe P. Mechanical deformation in silicon by micro-indentation. *J Mater Res* 2001;15(5):1500–7.
- [40] Tsukuda A, Kondo Y, Kuroshima Y, Uematsu K. Relationship between grinding mechanism and residual cracks in single point grinding test of alumina ceramics with different grit size. *J Ceram Soc Jap* 1995;103(3):268–73.
- [41] Lawn BR, Evans AG, Marshall DB. Elastic/plastic indentation damage in ceramics: the median/radial crack system. *J Am Ceram Soc* 1980;63(9–10):574–81.
- [42] Misra A, Finnie I. On the scribing and subsequent fracturing of silicon semiconductor wafers. *J Mater Sci* 1979;14:2567–74.
- [43] Jian SR, Chen GJ, Juang JY. Nanoindentation-induced phase transformation in (110)-oriented Si single-crystals. *Curr Opin Solid State Mater Sci* 2010;14:69–74.
- [44] Trachet A, Subhash G. Microscopic and spectroscopic investigation of phase evolution within static and dynamic indentations in single-crystal silicon. *Mater Sci Eng A* 2016;673:321–31.
- [45] Nakamura M, Sumomogi T, Endo T, Saiki T. The study on ductile mode cutting of single crystal silicon. *Hirosima Kokusai Gakuin Univ Rep* 1999;32:51–8.
- [46] Yan J, Syoji K, Kuriyagawa T, Suzuki H. Ductile regime turning at large tool feed. *J Mater Process Technol* 2002;121:363–72.
- [47] Arif M, Rahman M, San WY. Analytical model to determine the critical feed per edge for ductile-brittle transition in milling process of brittle materials. *Int J Mach Tools Manuf* 2011;51:170–81.
- [48] Shibata T, Fujii A, Makino E. Ductile-brittle transition during diamond turning of single-crystal silicon. *J Jap Soc Prec Eng* 1999;65(10):1512–6.
- [49] Ichida Y, Kishi K, Hasuda Y, Akbari J. Study on mirror finish grinding of fine ceramics (1st report)—Fundamental consideration on mechanism of surface generation. *J Jap Soc Prec Eng* 1991;57(8):98–104.
- [50] Yan J, Yoshino M, Kuriyagawa T, Shirakashi T, Syoji K, Komanduri R. On the ductile machining of silicon for micro electro-mechanical systems (MEMS) opto-electronic and optical applications. *Mater Sci Eng A* 2001;297:230–4.
- [51] Yan J, Syoji K, Kuriyagawa T. Chip morphology of ultra-precision diamond turning of single crystal silicon. *J Jap Soc Prec Eng* 1999;65(7):1008–12.
- [52] Arefin S, Li XP, Cai MB, Rahman M, Liu K, Tay A. The effect of the cutting edge radius on a machined surface in the nanoscale ductile mode cutting of silicon wafer. *J Eng Manuf* 2007;221:213–20.
- [53] Wu H, Melkote SN. Study of ductile-to-brittle transition in single grit diamond scribing of silicon: application to wire sawing of silicon wafers. *J Eng Mater Technol* 2012;134(041011):1–8.